ARTICLE OPEN

Check for updates

Investigation of non-uniform oxidation based on a mechanochemical phase field model with nonlinear reaction kinetics and large inelastic deformation

Chen Lin[1]✉, Jishen Jiang[1], Haihui Ruan[2]✉ and Xianfeng Ma[1]✉

A mechanochemical model is proposed to investigate the non-uniform oxidation of thermal barrier coatings (TBCs) that involves large inelastic deformation and nonlinear reaction kinetics. The large-deformation theory incorporates the higher-order term of geometric nonlinearity for a more precise description of the deformation and stress evolution in an oxide layer. The effect of stresses on the reaction kinetics is considered, which is expressed as the Eshelby stress tensor to account for the conformational volume change and deformation energy. A nonlinear reaction kinetics is adopted for a more accurate description of the nonequilibrium thermodynamic processes. The 2D simulations reveal a non-uniform oxide growth, three modes of oxide-metal interfacial morphology evolution, and tensile stress concentrations in the oxide scale. These simulation results agree with the experimental observations that cannot be described by the previous models. With the model, it is further demonstrated that a stable interfacial morphology and a significantly reduced tensile stress can be achieved by increasing the creep rate of the oxide and the flatness of the oxide-metal interface. This model thus provides an approach to extend the service time of TBCs.

npj Materials Degradation (2023)7:57 ; https://doi.org/10.1038/s41529-023-00376-z

INTRODUCTION

The mechanochemical coupling, involving the intrinsic interactions of diffusion, reaction, and mechanical deformation, plays a significant role in many material systems such as energy storage materials[1], chemically active materials[2], reaction-based self-healing materials[3], anti-corrosion materials[4–6], and high-temperature materials[7,8]. In the applications of these materials, a typical degradation process often starts from the adsorption of external 'guest atoms' on surfaces[9]. After the capture of free electrons, the guest atoms become ionized; meanwhile, some host atoms are also ionized by losing electrons. Combining guest and host ions leads to the reaction and forms a new phase. This reaction is maintained by the diffusion of guest and host ions, which may meet at the interfaces between the newly formed phase and the substrate or the free surfaces[10] due to the difference in the diffusion rates of host and guest ions. The combination reaction occurring at the new-phase surface leads to an outward growth of a new phase. If at the new-phase-substrate interface, it causes an inward growth of the new phase. The diffusion of ions and forming a new phase may lead to a deviation of the solid's composition from its stoichiometric composition. Such a deviation is usually accompanied by a volumetric change, which, if not appropriately accommodated, will develop a localized stress field. This stress field with a maximum magnitude as high as a few GPa[11] can be determined by measuring the change in the curvature of a specimen or from peak shifts in X-ray diffraction patterns or Raman spectra. It can also affect chemical potentials and alter the kinetics of diffusion and chemical reaction.

Experimental studies[12–14] have elucidated the relationship between stresses and reaction kinetics in a variety of disciplines. High-temperature oxidation of thermal barrier coating systems (TBCs) in a modern gas turbine engine is a typical example of such mechanochemically coupled problems. TBCs are deposited on superalloy turbine blades to enable the operation of a turbine at an extremely high temperature. Cooperation between film cooling and power generation has significantly increased energy conversion efficiency and reduced greenhouse gas (GHG) emissions[15]. Such a multilayer coating system consists of a metallic bond coating (BC), a thermally grown oxide (TGO), and a thermal-barrier ceramic (TC) layer. Among them, the TGO layer is formed as a result of the oxidation of a BC layer in service.

Spallation in TBCs severely limits the service life of a turbine engine, which is one of the critical problems of TBC arising from the growth of a TGO layer. As revealed in several experimental studies[16–18], metal-oxide interface roughening may occur due to the influence of mechanical stresses on the oxide growth. Such a heterogeneous growth of TGO is the consequence of morphological instability that occurs even when the initial BC and TGO are flat, and it is conceptualized that interface roughening leads to the formation of local separations that grow in size during thermal cycles.

Numerous studies have associated the failure mechanism of TBC with TGO growth. In most theoretical investigations, TGO thickness was assumed to be uniform[19–23]. However, a non-uniform growth of TGO, which occurs in experiments, can be an important factor. Bosso et al. [24] thus evaluated the impact of non-uniform oxidation during isothermal oxidation and after cooling. They established a theoretical model to describe elastoplastic and creep deformations of a TBC system with the assumption of significant volumetric strains due to oxide formation during an isothermal exposure. With this setting, their numerical results unveil significant out-of-plane tensile stresses along an interface, which increase with the waviness of the interface. Che et al.[25], Shen et al.[26], Li et al.[27], and Xie et al.[28] also examined the effect of the non-uniform growth of TGO on the evolution of interfacial stresses. It should be noted that in these stress analyses[24–28], the

[1]Sino-French Institute of Nuclear Engineering and Technology, Sun Yat-Sen University, Zhuhai, China. [2]Department of Mechanical Engineering, The Hong Kong Polytechnic University, Hong Kong, China. ✉email: linch67@mail.sysu.edu.cn; haihui.ruan@polyu.edu.hk; maxf6@mail.sysu.edu.cn

thickness of a TGO layer was presumed. Hence, the interplay between stress and growth remains unrevealed. As a stress state does influence chemical processes (diffusions and reactions), there is a need to develop a coupled model.

A rationalized thermodynamics framework can be the starting point to model a TGO with the complexity of coupled kinetic processes, such as diffusions, reactions, and mechanical deformation. It was pioneered by Larche and Cahn[29], who introduced a stress-dependent chemical potential. Since then, Bucci et al.[30], Bower et al.[31], Gao et al.[32], Haftbaradaran et al.[33], Huang et al.[34] and Zhou et al. [35] have applied this general framework to a variety of problems in materials engineering. The hydrostatic Cauchy stress enters stress-dependent chemical potentials in their formulae, and the diffusion equation depends on stresses. Wu[36] and Cui et al.[37] then developed a stress-dependent chemical potential formulation for finite deformation in which they adopted the Eshelby momentum tensor to replace the hydrostatic Cauchy stress.

Another issue is how to formulate the kinetics of a chemical reaction that involves the effects of various physical fields. An empirical kinetics equation may not satisfy the requirement of detailed balance[35–38]. For example, in many theoretical models[39–42], a reaction rate is assumed to be proportional to chemical potentials (the thermodynamic driving forces) following the conventional Onsager relations to minimize the free energy of a system. It, in principle, is only valid for systems close to equilibrium. In nonequilibrium processes, such linear expressions of reaction rates are inaccurate. For example, in modeling TGO, the liner chemical kinetics leads to a perplexing result that the growth of an oxide scale is almost unaffected by mechanical stresses, even when the growth stress is several GPa (see Fig. 15a in ref. [39] and Fig. 11 in ref. [40]) because the contribution of mechanical energy to driving forces is significantly less than that of chemical energy. In addition, a chemical reaction often occurs at interfaces between reactants and products and drives interfaces to migrate. It is easy to theorize for the problems with flat interfaces but becomes difficult for problems with curved and evolving interfaces.

An interface-migration mechanochemical problem may be best treated by involving diffusive interfaces, which gives rise to the phase-field (PF) method that replaces the traditional method involving a complex interface-tracking technique. The phase indices are field variables that vary continuously across interfaces and evolve based on chemical reaction kinetic equations. This treatment makes it possible to deal with complex morphology evolution without tracking interface positions explicitly[7,8,41–43]. As above-mentioned, numerous efforts have been devoted to the theoretical study of oxidation for advanced materials and structures. Additional research, however, is still required to elucidate how reaction kinetics and thermodynamic driving forces can be related to systems that are highly out of equilibrium and how the reactions lead to morphology change and large inelastic deformations.

This paper proposes a mechanochemical model with the main effort of formulating reaction kinetics and large inelastic deformations. We strive to make the formulae conform to the requirement of the detailed balance of a reaction, which applies to systems close to equilibrium and those far from equilibrium when the thermodynamic driving force is significant. The Helmholtz free energy is expressed as the sum of chemical potential, interfacial energy, and mechanical strain energy to incorporate large inelastic deformations. Then thermodynamic driving forces can be calculated based on the variational derivatives of the total free energy with respect to the corresponding field variables. We assume the equivalence of reaction rate and phase transformation rate; then, the equation governing oxide growth is expressed as a generalized Allen-Cahn equation. Finally, the PF model is completed by combining the Allen-Cahn, diffusion-reaction, and mechanical equilibrium equations. The corresponding numerical solutions lead to roughened TGO/BC interfaces and tensile stresses, which is the reason for the cracking and failure of a TBC.

RESULTS

The detailed parameters, the geometries as well as the initial and boundary conditions used in the simulation are described in the Supplementary information.

1D mechanically-chemically coupled oxidation simulation

In this work, we only consider the most stable oxide scale (Al_2O_3) developed on an Al-containing BC (e.g., FeCrAlY); hence, $n = 2/3$. We first illustrate the effect of stress on oxide growth through one-dimensional (1D) simulations. Shown in Fig. 1a is the variation of the oxide scale thickness, h_{ox}, with the square root of time, $t^{0.5}$, for various eigenstrains, ε_m^{eg}. When the eigenstrain is small, h_{ox} varies linearly with $t^{0.5}$, which is expected based on Wagner's one-dimensional (1D) theory that describes a diffusion-mediated process. However, as the eigenstrain increases, the thickness change of the oxide scale gradually deviates from Wagner's theory and becomes more curved. It is noted that in the early stage of oxidation, the rate of increase in h_{ox} with respect to $t^{0.5}$ is significantly reduced under a large ε_m^{eg}. As oxidation continues, the slope of the curve gradually increases and reaches a constant value. This constant value is also debased by increasing ε_m^{eg}. According to Eq. (38) (Section 3.3), the stresses at the oxide-metal interfaces influence the chemical potentials of reaction. Figure 1b illustrates the distribution of the in-plane stress, σ_{11}, along the depth at different times for the case of $\varepsilon_m^{eg} = 0.08$. As oxidation advances with time, stress is relaxed due to creep deformation, resulting in a decrease in the maximum compressive stress near the interface. Such a decrease promotes the oxidation reaction, causing the increase in the slope of h_{ox} with $t^{0.5}$.

Due to the inhomogeneous and time-varying distribution of interfacial stresses, we use the spatial-temporal average to evaluate the stress contribution to the reaction driving force under various theoretical assumptions, which is defined as:

$$\tau_{\sigma,m} = \frac{\int_t \int_{y|_{\phi=0.95}}^{y|_{\phi=0.05}} \tau_\sigma dy dt}{\delta t_0} \tag{1}$$

Where y denotes the depth from oxide surface, $t_0 = 400$ h is the total oxidation time. Figure 1c shows the variations of the dimensionless stress contribution term, $\tau_{\sigma,m}/(RT)$, with the square of eigenstrain, $(\varepsilon_m^{eg})^2$, obtained under four different assumptions:

(I) large deformation (Eq. (30) in Section 3.2) and nonlinear reaction kinetics (Eq. (39) in Section 3.3),
(II) small deformation (Eq. (31) in Section 3.2) and nonlinear reaction kinetics (Eq. (39) in Section 3.3),
(III) large deformation (Eq. (30) in Section 3.2) and linear reaction kinetics (Eq. (42) in Section 3.3), and
(IV) small deformation (Eq. (31) in Section 3.2) and linear reaction rate (Eq. (42) in Section 3.3).

It is noted that the stress contribution to the reaction driving force increases with the eigenstrain, which is approximately linearly dependent on $(\varepsilon_m^{eg})^2$. In addition, when the eigenstrain is large, the mechanical contribution to the reaction driving force is more significant under the small-deformation assumption than those under the large-deformation assumption. It is the consequence of the negligence of the conformal volume change in the small-deformation theory (as expressed in Eq. 31 in Section 3.2) and the higher-order term of nonlinear deformation in the constitutive relationship.

With the average stress contribution term $\tau_{\sigma,m}$ the corresponding average reaction rate for nonlinear reaction kinetics can be

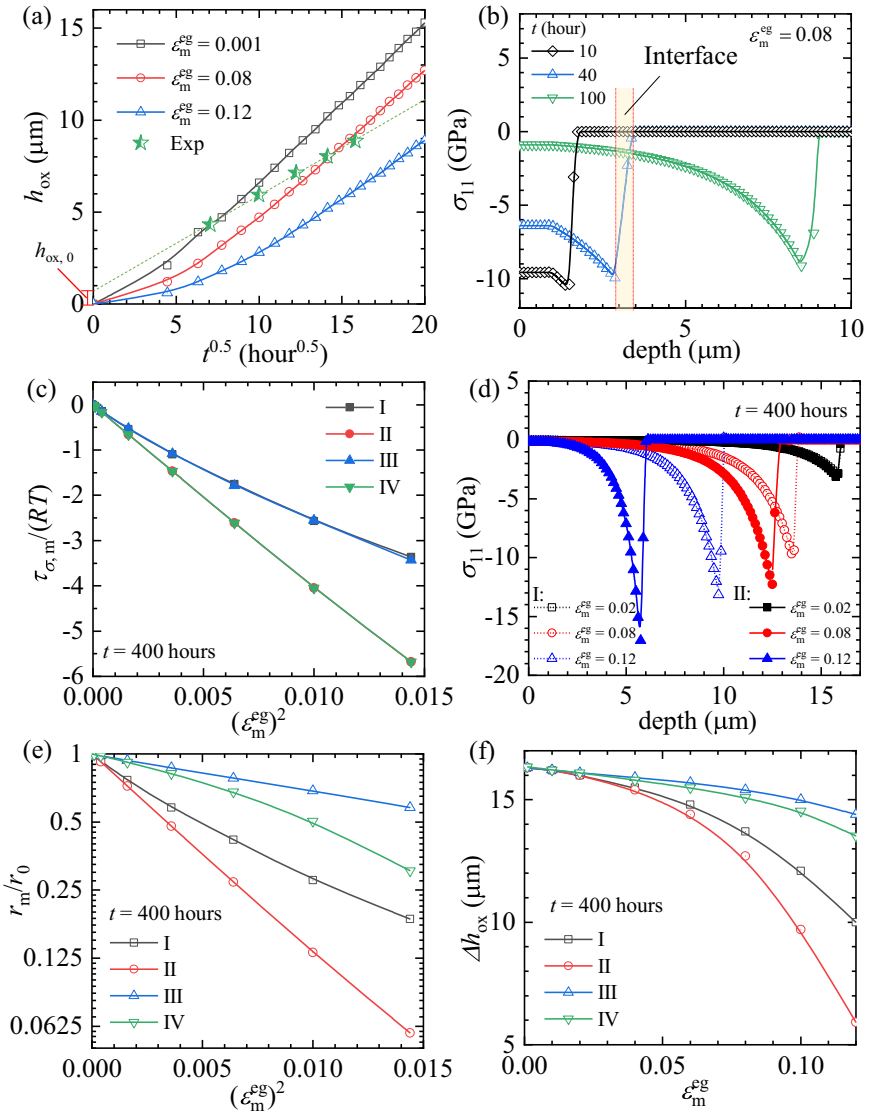

Fig. 1 Results of a 1D numerical model. a Variations of oxide scale thickness, h_{ox}, with the square root of time, $t^{0.5}$, for various eigenstrains, ε_m^{eg}, **b** the distribution of the in-plane stress, σ_{11}, and the order parameter, ϕ, along the depth at different times for $\varepsilon_m^{eg} = 0.08$; (**c**, **e**, **f**) the variations of the dimensionless stress contribution term, $\tau_{\sigma,m}/(RT)$, the dimensionless reaction rate, r_m/r_0, and the oxide film thickness, h_{ox}, with the square of eigenstrain, $(\varepsilon_m^{eg})^2$, under four theoretical assumptions; (**d**) the distribution of the in-plane stress, σ_{11}, for $\varepsilon_m^{eg} = 0.08$, under various theoretical assumptions. Herein, the four assumptions are: (*I*) large deformation and nonlinear reaction rate, (II) small deformation and nonlinear reaction rate, (III) the case of large deformation and linear reaction rate, and (IV) small deformation and linear reaction rate.

defined as:

$$r_m = L_\eta \left(\frac{c_O}{c_O^{ref}}\right)^n \left(\exp\left(\frac{(1-\rho)(n\mu_O^0 + \tau_{\sigma,m})}{RT}\right) - \exp\left(-\frac{\rho(n\mu_O^0 + \tau_{\sigma,m})}{RT}\right)\right) \quad (2)$$

and for linear reaction kinetics is

$$r_m = L_\eta^* \left(\frac{c_O}{c_O^{ref}}\right)^n \left(\frac{n\mu_O^0 + \tau_{\sigma,m}}{RT}\right) \quad (3)$$

The effect of stress on reaction rate under various theoretical assumptions can then be compared in Fig. 1e that illustrates the variations of the dimensionless average reaction rate, r_m/r_0, (r_0 is the reaction rate without a stress effect) with $(\varepsilon_m^{eg})^2$ under the four theoretical assumptions. It can be observed that with the assumption of linear reaction rate, the stress effect is much less than that based on the nonlinear equation. Figure 1f demonstrates that when a linear reaction rate is assumed, the effect of stress on oxide growth remains minimal even when the eigenstrain reaches 0.12, which cannot explain the experimental results of Ramsay et al.[12] and Platt et al.[16]. This indicates the inadequacy of the traditional linear relation between the reaction rate and driving force. Instead, with the nonlinear equation, the small stress contribution can significantly affect oxide growth, as demonstrated by the red and black lines in Fig. 1f.

Comparison of four assumption in 2D cases

We then investigated the high-temperature oxidation of a BC with a surface groove (The groove comprises two arcs with the radius of curvature R_1 and R_2, constrained by $R_1 + R_2 = 25$ μm, see details in Supplementary Fig. 1) following ref. [44]. Figure 2a shows the morphological changes of the surface groove after 40 h of oxidation. As a result of stress concentration, the top of the groove is elevated by δ_1, while the bottom is depressed by δ_2. It results in an increase of $\Delta A = \delta_1 + \delta_2$ in the overall depth of the

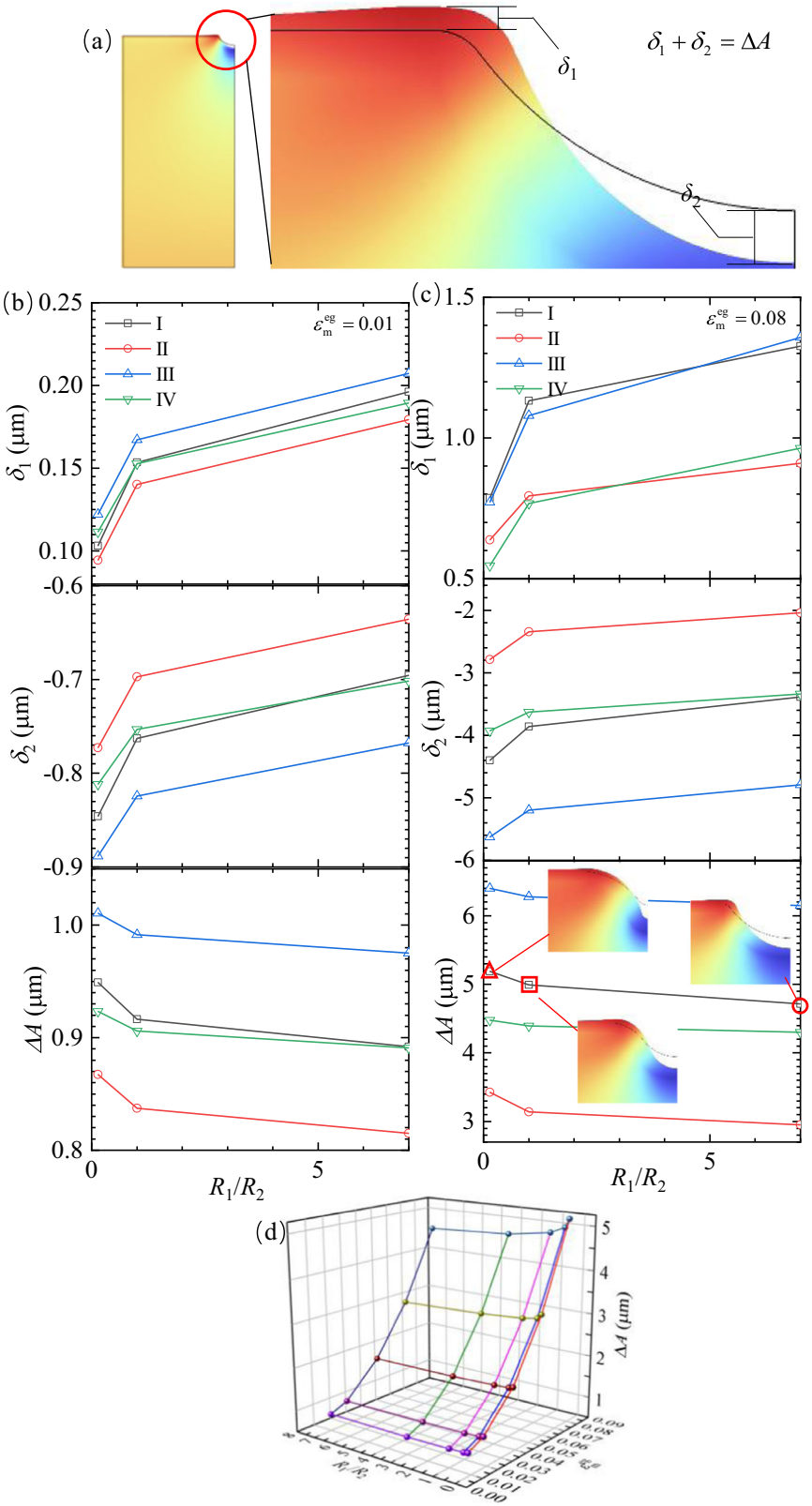

Fig. 2 Simulation results of the oxidation of the FeCrAlY plate with a surface grooves. a Morphological changes of surface grooves after 40 h of oxidation; **b**, **c** the changes in the groove's top, bottom, and overall depth after 40 h of oxidation under different theoretical assumptions, for $\varepsilon_m^{eg} = 0.01$ and 0.08, respectively; and (**d**) the evolution of groove's overall depth with ε_m^{eg} and R_1/R_2.

groove. These changes are then quantified in Fig. 2b, c for $\varepsilon_m^{eg} = 0.01$ and 0.08, respectively. As R_1/R_2 increases, the top of the groove becomes more curved, while the bottom becomes less curved, causing greater stress concentration at the top and less at the bottom. It lifts the hump at the top and decreases the depression of the groove, ultimately reducing its overall depth. Since the higher-order term of nonlinear deformation is considered using the large-deformation theory, the change in the morphology of the oxidized groove is more significant than those obtained under the small-deformation assumption, especially when the eigenstrain is large. In addition, when the linear reaction rate is assumed, the change in surface morphology after oxidation is more pronounced than that based on the nonlinear reaction rate, because oxidation is less affected by stress under the linear assumption. The latter results in a prediction of thicker oxide films and higher internal pressure. The evolution of the overall depth of the groove, ΔA, with volumetric eigenstrain, ε_m^{eg}, and the geometry of the surface groove, R_1/R_2, is also shown in Fig. 2d. It is observed that compared to the effect of surface groove geometry, the effect of volumetric eigenstrain on fold deformation is more significant. Moreover, the overall depth of the groove increases in an accelerated rate with the increasing of volumetric eigenstrain. It is because, with the increase of the volumetric eigenstrain, the effect of the higher-order term of nonlinear deformation becomes more significant, making the change in the geometry of the oxidized scratches more obvious.

A significant tensile stress field in a TGO is the root cause of its failure. Hence, let us emphasize how large tensile stress is developed during oxide growth. Figure 3 shows the maximum tensile stress in the in-plane direction, $\sigma_{11,\,max}$, from the bottom to the top of the groove with the increase in R_1/R_2. Compared with the result of the linear reaction kinetics (cases III and IV), the inhomogeneous growth of the oxide film under the nonlinear reaction kinetics (case I and II) results in more significant tensile stresses at the top, which is more likely to initiate cracks. This model can thus explain the experimentally observed vertical cracks in an oxide film[45,46]. Note that the highest tensile stress in the out-of-plane direction, $\sigma_{22,\,max}$, is located at the top of the groove near the oxide-metal interface. It suggests transverse cracks at the oxide-metal interface near the groove's apex and propagate along the interface, resulting in the peeling of the oxide film. Moreover, as R_1/R_2 increases, the curvature at the top of the groove increases, leading to a greater concentration of interfacial tensile stress, as shown in Fig. 3. It is noted that the maximum σ_{22}

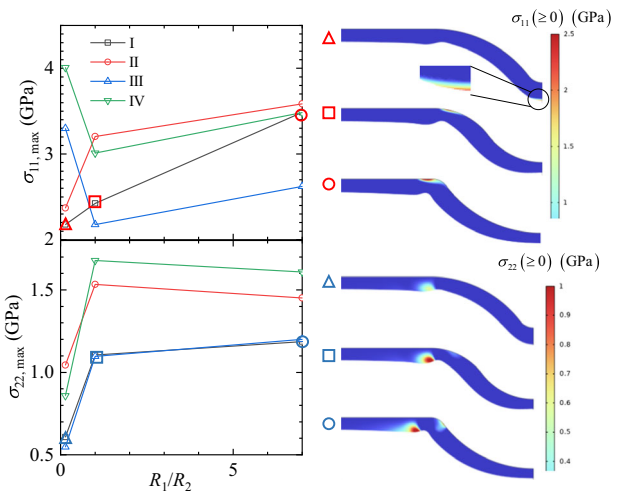

Fig. 3 Evolution of maximum tensile stress in oxide film. The evolution of maximum tensile stress in the 11 (in-plane) and 22 (out-of-plane) directions after 40 h of oxidation with R_1/R_2, for $\varepsilon_m^{eg} = 0.08$, under different assumptions.

predicted under the assumption of linear reaction rate is much larger than those predicted under the nonlinear assumption. Because the transverse normal stress σ_{22} is associated with the interface morphology and the oxide film thickness, the assumption of a linear reaction rate leads to a thicker oxide film and, thus, a higher internal pressure. They bring a more prominent hump at the top of the groove, thereby causing a larger σ_{22} at the interface near the hump.

2D simulation of high-temperature oxidation of TBCs

We now consider a complete TBC system involving TC, TGO, and BC; among them, the TC layer is molded as an elastic solid on top of the TGO. We simulated TGO growth and stress evolution based on the four assumptions and discussed their effects in this section. As shown in Fig. 4a, with the increase in eigenstrain the average thickness of TGO, $h_{ox,\,m}$, decreases. Moreover, the TGO thickness predicted based on a nonlinear oxidation rate is smaller than that predicted based on a linear oxidation rate. It conforms to the simulation results mentioned above. In addition, comparing the linear and nonlinear oxidation rate, the change in the morphology of the TGO-BC interface is more pronounced in the latter case when the eigenstrain increases, i.e., the waviness of the TGO-BC interface increases with the increase of eigenstrain especially under a nonlinear oxidation rate. Such a non-uniform growth of TGO is caused by the non-uniform distribution of compressive stress within the film, which is concentrated at the peaks of the TGO-BC interface. Therefore, the effect of interfacial stress on the oxidation rate is non-uniform. It leads to slower growth of the oxide film near an interfacial peak and the formation of a non-uniform oxide film. Such a non-uniform TGO can be better predicted when a nonlinear oxidation rate is assumed, leading to consistency with the experimental findings[12,16,47]. Note that this is not the case when adopting a linear oxidation rate.

Since a large number of experimental studies have confirmed that the failure of TBCs is usually the result of interface spalling due to crack initial and propagation within the TC layer[48,49], in this section, the tensile stress evolution within the TC layer is studied carefully. As shown in Fig. 4b, the maximum (tensile) σ_{11} and σ_{22} in the TC layer are located at the peak and valley of the TC-TGO interface. They can bring about two possible fracture modes within the TC layer: forming vertical cracks at the peak of the TC-TGO interface and causing an interlayer fracture at the valley of the TC-TGO interface. They were both observed experimentally in the TC layer[48]. Furthermore, the tensile stresses predicted by assuming the nonlinear reaction rate are more significant and likely to induce cracking than those predicted by the assumed linear reaction rate.

Some experiments have also confirmed that cracking occurs not only in the TC layer but also in the TGO layer[45,46]. Therefore, the tensile stress evolution in TGO is also studied, as shown in Fig. 4c. Assuming a nonlinear reaction rate, the maximum σ_{11} occurs at the TC-TGO interface peak. It is the reason for the vertical cracks in a TGO that has been experimentally observed[45,46]. Assuming the linear reaction rate cannot lead to such a result because the non-uniform growth of TGO is caused by the nonlinear oxidation kinetics that is more sensitive to stresses. This non-uniform growth makes the oxide film bend, resulting in the maximum σ_{11} at the peak of the oxide film. When the eigenstrain increases, the maximum σ_{22} in the TGO increases, and the location of the maximum σ_{22} shifts from the TC-TGO interface valley to a location close to the TGO-BC interface peak. This change implies two potential locations for crack initiation in the transverse direction in a TGO film: either at the TC-TGO interface valley or near the TGO-BC interface peak; both of them were indeed observed in the experiments[48,49].

Numerous studies have shown that the interfacial geometry and intrinsic mechanical properties affect a TBC's oxidation

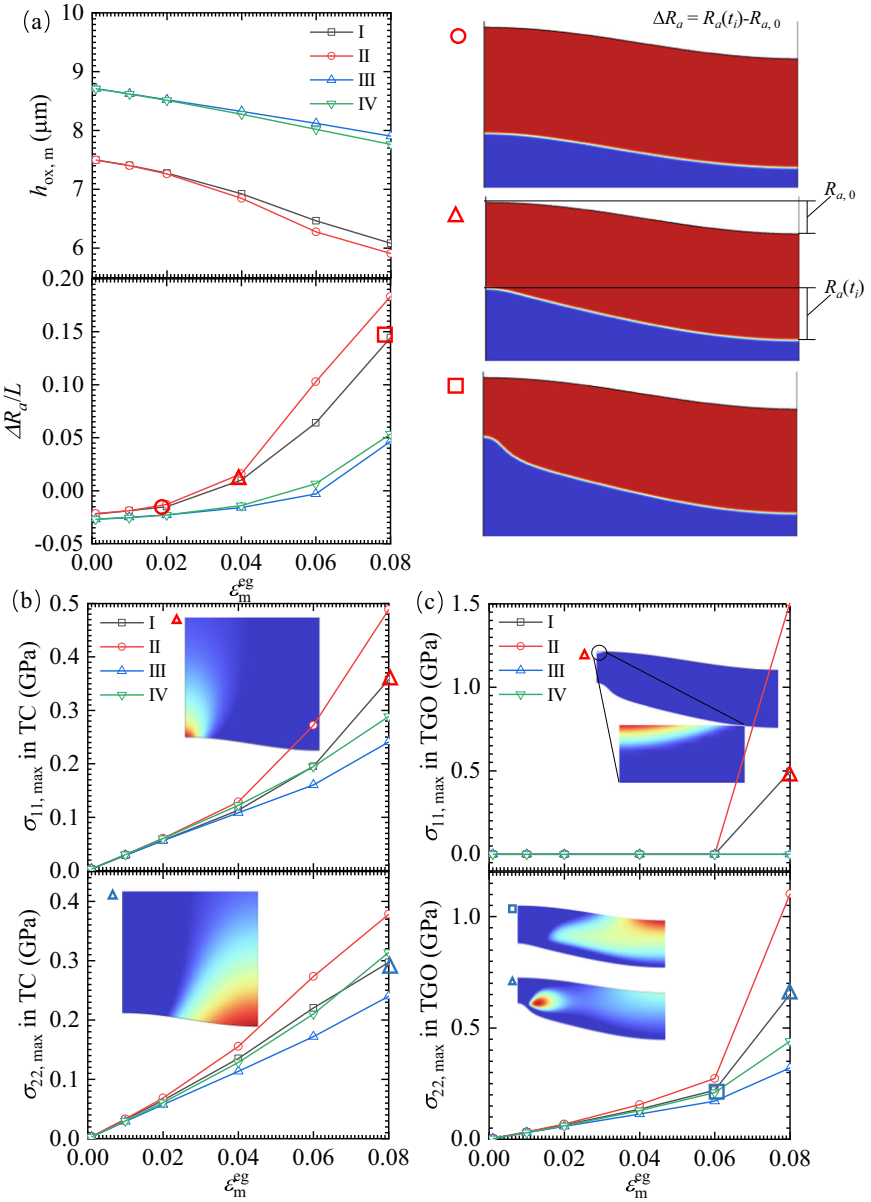

Fig. 4 2D simulation results of a TBC with a sinusoidal interface. a The variation of average thickness of TGO, $h_{ox,\,m}$, after 100 h oxidation, with eigenstrain, under different theoretical assumptions; (**b**, **c**) the variations of the maximum tensile stress after 100 h oxidation with eigenstrain within the TC and TGO layers, respectively, under different theoretical assumptions.

behavior and stress evolution. Thus, a strategy to optimize a TBC's service life is modulating the interface morphology and mechanical properties. This is uneasy in experiments but can be studied based on the mechanochemical PF model and the assumptions of nonlinear reaction and large deformation, which have shown the ability to reveal experimental findings.

Figure 5 shows how the average thickness of TGO and the waviness of the TGO-BC interface vary with time for various initial geometries. In the figure, $R_{a,0}$, and L denote the sinusoidal interface amplitude and wavelength, respectively, and $R_{a,0}/L$ is the ratio that characterizes the non-dimensional interface roughness. As demonstrated in Fig. 5(a, b), the average thickness of TGO increases with the increase in $R_{a,0}/L$, which is consistent with the experimental finding[16]. It is because increasing the initial interfacial roughness increases the specific surface area of the oxidation front; the oxidation reaction is then accelerated. Fixing $R_{a,0}/L$, and increasing (or decreasing) L do not affect the specific surface area of the oxidation front and, consequently, the average thickness of TGO.

As shown in Fig. 5c, different initial interface morphologies can result in very different roughness evolutions of the TGO-BC interface, which are the results of competition between two competing mechanisms arising from an interfacial bulge. On the one hand, an initial interfacial bulge increases the specific surface area of the reaction. As shown in Fig. 5c, oxygen concentration distribution along the TGO-BC interface becomes more and more inhomogeneous with the increase of the initial interface bulge. Herein, at the peak of the bulge, the increase in the specific surface area leads to a higher oxygen concentration, while at the valley decrease in the specific surface area leads to a lower oxygen concentration. Consequently, faster oxidation occurs at the peak, which results in a flattening of the interface bulge. On the other hand, the bulge causes stress concentration and inhibits local oxidation that tends to roughen the interface. Therefore, the evolution of TGO-BC interface roughness can have three trends

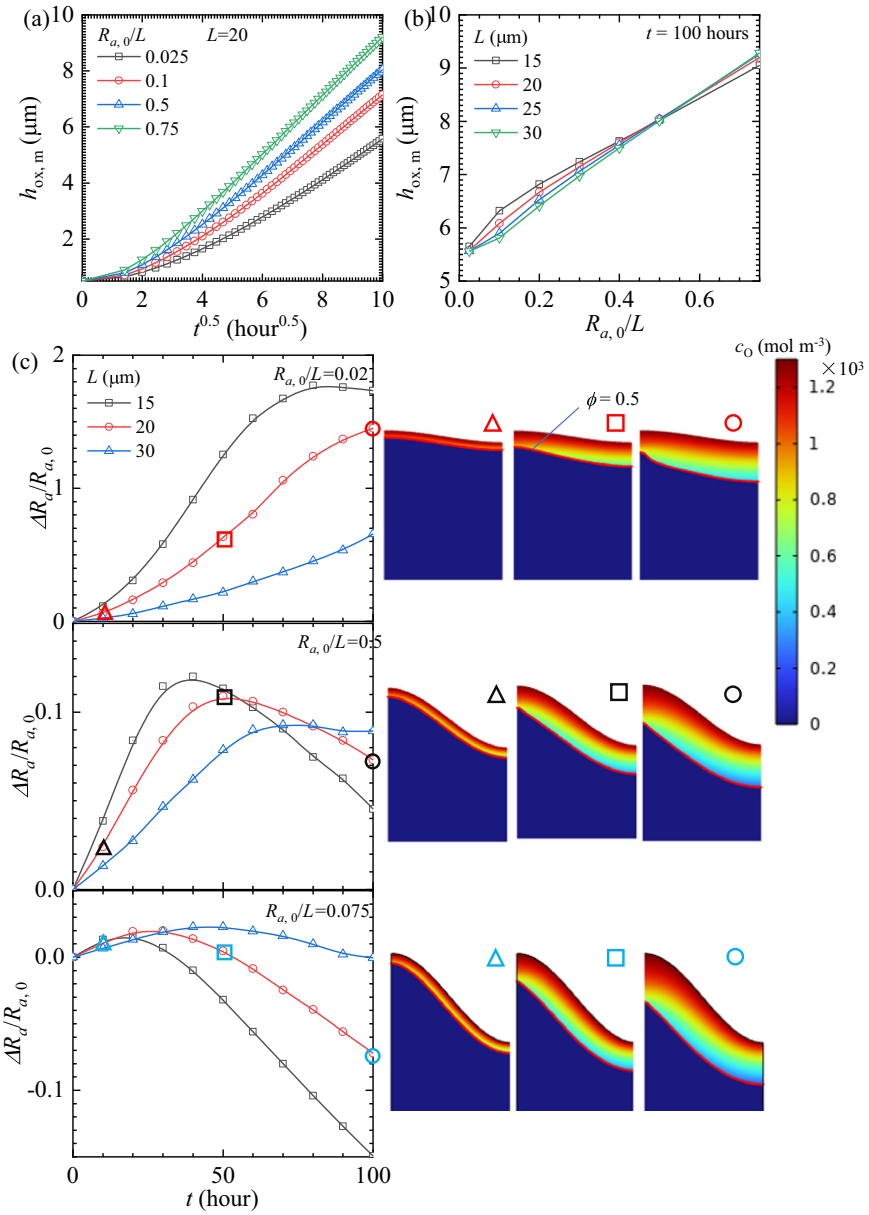

Fig. 5 Simulation results of the TGO growth. a Evolution of thickness of TGO with time for various initial geometries; **b** the average thickness of TGO after 100 h oxidation with the initial amplitude-to-wavelength ratio of interface; **c** the evolution of oxidation interface roughness, which shows three pattern evolutions; and the oxygen concentration distributions for different time and initial geometries are also shown in Fig. 5c.

during oxidation: (1) increasing with oxidation time, (2) increasing and then decreasing, and (3) decreasing continuously. Existing experimental observations[16] have corroborated these trends revealed by our model. In addition, our simulations show that increasing the interface wavelength can significantly reduce the change of the interface roughness, which can be a way to stabilize the interface morphology.

Since the failure generally occurs inside the top coating, the impact of oxidation on the tensile stress evolution in the TC layer is studied. Figure 6a shows the evolutions of tensile stresses within the TC with oxidation time affected by several initial geometries. In accordance with the simulation results presented previously, the tensile stresses in the in-plane and out-of-plane directions in the TC layer are concentrated in the peaks and valleys of the TC-TGO interface, respectively. In addition, the maximum tensile stresses increase and gradually decrease with oxidation time. It is due to the competing effects of oxide growth and creep. In addition, the evolutions of tensile stresses in the TGO with oxidation by several initial geometries are also evaluated, as shown in Fig. 6b. It is also observed that the maximum tensile stress in the in-plane direction σ_{11} increases and then decreases due to TGO growth and creep. Instead, the maximum σ_{22} first increases gradually and then steeply. It is the result of stress redistribution caused by the non-uniform growth of the oxide film.

Since the creep rate of TGO can span several orders of magnitude by the grain size or alloy composition variation and increasing the creep rate can significantly reduce the growth stress, the non-uniform growth of TGO can thus be mitigated by creep. Figure 7 shows the effect of creep rate on the average thickness of TGO, the change in TGO-BC interface roughness, and the maximum tensile stress within the TC and TGO layers after 100 h of oxidation based on several initial TGO-BC interface waviness. It is shown that increasing the TGO creep rate, decreasing the initial interface roughness ($R_{a,0}/L$), and increasing

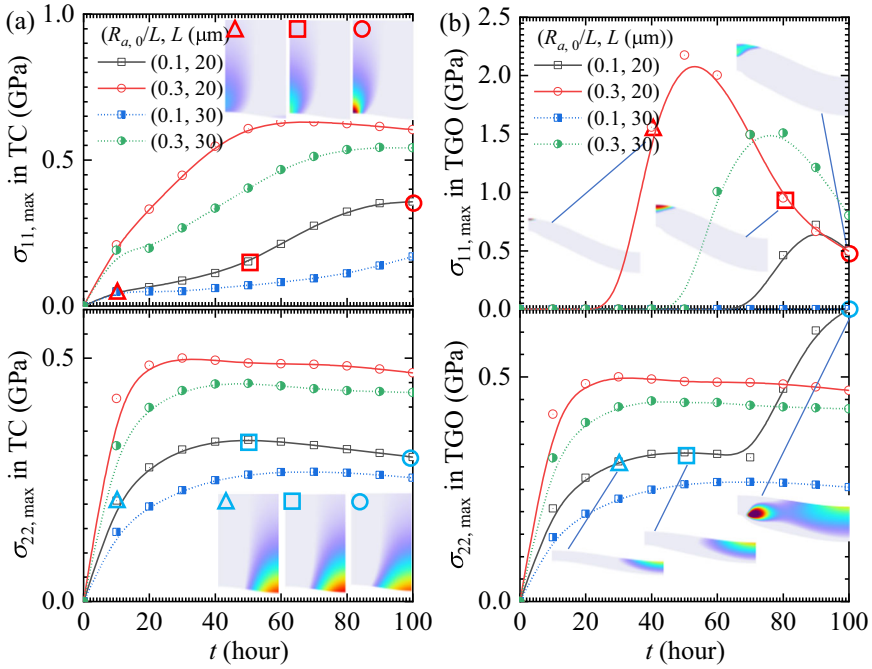

Fig. 6 Evolution of maximum tensile stress in TBCs. The evolution of the maximum tensile stress in (**a**) TC and (**b**) TGO with time for various initial geometries.

the wavelength (L) can significantly improve the stability of the interface morphology and reduce the tensile stress during oxidation. They form a strategy to extend the service life of TBC in extreme service environments, i.e., regulating the initial interface geometries and the creep rate of TGO by improving the plasma vapor deposition process and varying the grain size or alloy composition, respectively.

DISCUSSION

This paper proposes a phase field model to deal with large deformations, nonlinear oxidation kinetics, and their interplay in a thermodynamical framework. The relation between stresses and reaction driving forces is established based on the variational derivatives of the free energy with respect to phase field variables. The stress contribution term is expressed as the Eshelby stress tensor, which can involve the effects of conformational volume changes and higher-order terms of nonlinear deformation. Considering the detailed balance of a reactive system, the generalized BV equation is employed to describe nonequilibrium thermodynamic processes. Based on the developed model, oxidation simulations of metals and TBCs were carried out, which leads to the following conclusions.

1. The finite-deformation theory and nonlinear reaction kinetics are necessary to correctly capture the key phenomena in TGO cracking and interface roughness variation. For example, the assumption of small deformation ignores the higher-order terms of nonlinear deformation, leading to a smaller oxide film deformation and larger growth stress. The predicted oxide film growth rate is also lower because the effect of conformational volume change and deformation energy on the reaction is not taken into account. Because the contribution of mechanical energy is much less than chemical energy in a reaction potential, the linear reaction kinetics is extremely insensitive to stress. This problem is resolved with the nonlinear reaction kinetics.
2. The initial BC-TGO interface morphology and their mechanical properties affect the growth and stress evolution of TGO. It is caused by the competition between curvature (specific area) dependence and stress dependence when the BC-TGO interface is rough. The mechanochemical coupling and the nonlinear reaction kinetics lead to the nonuniform growth of the oxide film, which induces tensile stress concentrations in the in-plane and out-of-plane directions near the TGO humps. These are consistent with the crack locations observed in experiments. In contrast, when the mechanochemical coupling is ignored, or if this effect is small (e.g., with linear reaction kinetics), an oxide film grows uniformly and does not produce tensile stress concentrations near TGO humps.
3. A parametric study of the effects of TGO creep rate and interface morphology shows that increasing the TGO creep rate, decreasing the initial oxidation interface roughness, and increasing the sinusoidal interface wavelength can significantly improve the stability of the interface morphology and reduce the tensile stress during oxidation. This know-how could lead to a strategy to extend the service life of TBCs under extreme conditions. For example, regulating the initial interface geometries by improving the plasma vapor deposition process or increasing the creep rate of TGO by the grain size or alloy composition variation.

METHODS

Constitutive relationship considering large deformation

As shown in Fig. 8, let B be a solid with a fixed initial configuration, Ω_0. A motion of B is defined by a smooth one-to-one function, $\mathbf{u}(\mathbf{X}) = \mathbf{x}(\mathbf{X}) - \mathbf{X}$, that maps each material point $\mathbf{X}$ of B into a point $\mathbf{x}$ which is positioned in the current configuration denoted by Ω. Following Cui et al.[37], three Cartesian coordinate systems $\{e_I,e_J,e_K\}$, $\{e_i,e_j,e_k\}$ and $\{e_i,e_j,e_k\}$ have been used in the initial, intermediate and the current configurations, respectively, where the first two are the Lagrangian coordinate systems and the last one is the Eulerian coordinate system. Thus, the deformation gradient of material is expressed as $\mathbf{F} = \partial\mathbf{x}/\partial\mathbf{X} = \mathbf{I} + \nabla_{\mathbf{X}}\mathbf{u}$, where $\mathbf{I}$ is the Second-order identity tensor; $\nabla_{\mathbf{X}}$ is the gradient operator with

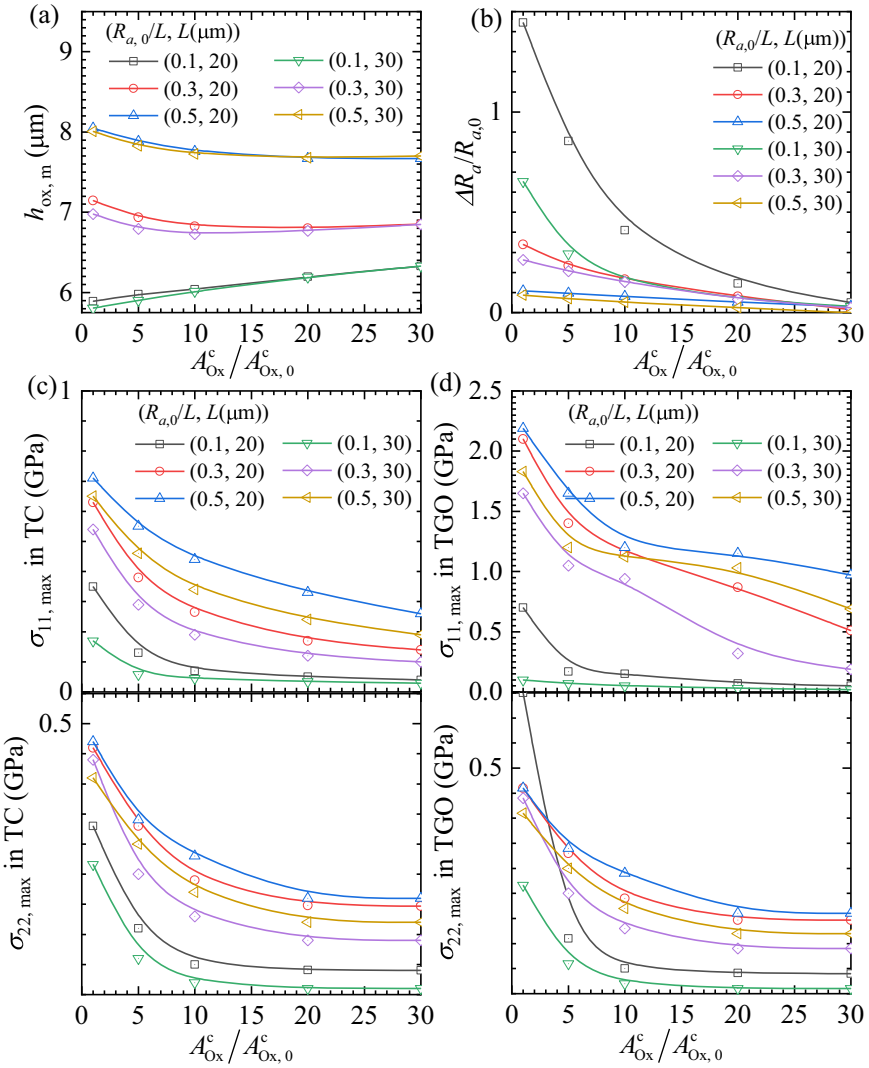

Fig. 7 Effect of creep on the TGO growth and maximum tensile stress in TBCs. The evolution of (**a**) the maximum average thickness of TGO, (**b**) the maximum roughness change for TGO-BC interface, the maximum tensile stress in (**c**) TC and (**d**) TGO during oxidation, with the variation of initial geometry of TGO-BC interface and the creep rate of TGO.

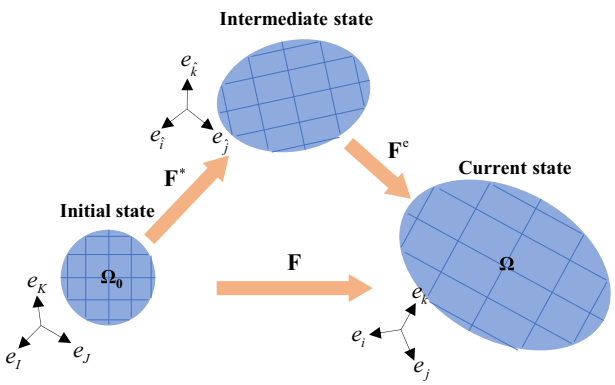

Fig. 8 Schematics of the initial, intermediate and current configurations. The $\{e_I,e_J,e_K\}$, $\{e_i,e_j,e_k\}$ are the Lagrangian coordinate systems and the $\{e_i,e_j,e_k\}$ is the Eulerian coordinate system.

respect to **X**. The main hypothesis underlying the finite strain constitutive theory is to decompose the deformation gradient, **F** in a multiplicative manner:

$$\mathbf{F} = \mathbf{F}^e\mathbf{F}^* \tag{4}$$

where $\mathbf{F}^e$ and $\mathbf{F}^*$ are the deformation gradient caused by elastic and inelastic deformation, respectively. In Fig. 1, an intermediated state is shown, which is transformed from the initial one by multiplying the deformation gradient tensor $\mathbf{F}^*$.

We then consider the following deformation gradients: (i) volumetric eigenstrain resulting from the change in specific volume when a metal M transforms into its oxide MO_n, denoted by $\mathbf{F}^{eg}$, (ii) the chemical expansion (or stoichiometric expansion) owing to the increasing fraction of diffusive element dissolved interstitially in the host lattice during diffusion, denoted by $\mathbf{F}^{ch}$, and (iii) the high-temperature creep of the stressed solid, denoted by $\mathbf{F}^{cr}$. The inelastic deformation gradient tensor, $\mathbf{F}^*$, can be further decomposed as follows:

$$\mathbf{F}^* = \mathbf{F}^{cr}\mathbf{F}^{ch}\mathbf{F}^{eg} \tag{5}$$

Following Zhao et al.[41], the deformation gradient caused by volumetric eigenstrain, $\mathbf{F}^{eg}$, can be expressed as:

$$\mathbf{F}^{eg} = (1 + h(\phi)\frac{V_{MO_n} - V_M}{V_M})^{\frac{1}{3}}\mathbf{I} = (J^{eg})^{\frac{1}{3}}\mathbf{I} = \varepsilon_m^{eg}\mathbf{I} \tag{6}$$

where as V_{MO_n} and V_M are the ionic volumes of oxide and metal, respectively, ε_m^{eg} is the volumetric eigenstrain, $h(\phi) = \phi^3(10 - 15\phi + 6\phi^2)$ is the interpolation function that varies from one to zero across the interface and herein ensures that volumetric eigenstrain only occurs in the oxide phase. $\phi \in [0, 1]$ is the order parameter to identify the oxide ($\phi = 1$) and metal ($\phi = 0$) phases, which corresponds to the concentration of oxide, c_{MO_n}, and its reference value, $c_{MO_n}^{ref}$, as $\phi = c_{MO_n}/c_{MO_n}^{ref}$. J^{eg} in Eq. (6) represents the change of molar volume during oxidation and $\mathbf{I}$ is the second-order identity tensor.

Following Ref. [37], the deformation gradient caused by chemical expansion, $\mathbf{F}^{ch}$, can be expressed as:

$$\mathbf{F}^{ch} = (1 + 3\eta c_O)^{\frac{1}{3}}\mathbf{I} = (J^{ch})^{\frac{1}{3}}\mathbf{I} \tag{7}$$

where c_O is the concentration of oxygen and η is the partial molar volume change due to the increase in the fraction of diffusive oxygen dissolved interstitially in the host lattice of the oxide. The latter can be experimentally determined using thermogravimetric analysis (TGA) under a controlled atmosphere[50].

We employ the Norton power law to describe the relation between creep strain rate and stress, which is expressed as:

$$\mathbf{D}^{cr} = A\left(\frac{\sigma^{eq}}{\sigma_{ref}^{eq}}\right)^n \frac{\partial \sigma^{eq}}{\partial \boldsymbol{\sigma}} \tag{8}$$

where $\mathbf{D}^{cr}$ is the rate of creep, expressed as $\mathbf{D}^{cr} = (\partial \mathbf{F}^{cr}/\partial t)\mathbf{F}^{cr-1}$, σ^{eq} and σ_{ref}^{eq} are the equivalent stress and its reference value, respectively. In Eq. (8), $A = h(\phi)A_{MO_n,0}^c + (1 - h(\phi))A_{M,0}^c$, $n = h(\phi)n_{MO_n} + (1 - h(\phi))n_M$ are the creep rate coefficients that vary continuously from metal to oxide with the interpolation function $h(\phi)$,.

The stress-strain relation can be derived within a thermodynamic framework via the entropy imbalance of system. Ignoring heat transfer, the entropy imbalance can be expressed as:

$$\frac{\partial W^{ext}}{\partial t} - \frac{\partial \psi^{mech}}{\partial t} = \frac{\partial S}{\partial t}T \geq 0 \tag{9}$$

where W^{ext}, ψ^{mech} and S are the rate of external power, electric energy and entropy densities, respectively, and T is the thermodynamic temperature. The rate of external power can be expressed as:

$$\begin{aligned} \dot{W}^{ext} &= \mathbf{P} : \frac{\partial \dot{\mathbf{F}}}{\partial t} \\ &= \mathbf{P} : \left(\frac{\partial \dot{\mathbf{F}}^e}{\partial t}\mathbf{F}^{cr}\mathbf{F}^{ch}\mathbf{F}^{eg} + \mathbf{F}^e\frac{\partial \dot{\mathbf{F}}^{cr}}{\partial t}\mathbf{F}^{ch}\mathbf{F}^{eg} + \mathbf{F}^e\mathbf{F}^{cr}\frac{\partial \dot{\mathbf{F}}^{ch}}{\partial t}\mathbf{F}^{eg} + \mathbf{F}^e\mathbf{F}^{cr}\mathbf{F}^{ch}\frac{\partial \dot{\mathbf{F}}^{eg}}{\partial t}\right) \end{aligned} \tag{10}$$

where $\mathbf{P}$ is the first Piola-Kirchhoff stress tensor. The elastic strain energy density per unit volume of the initial state can be expressed as:

$$\psi^{mech} = J^* \psi_0^{mech} = J^{ch}J^{eg}\left(\frac{1}{2}\mathbf{E}^e : \mathbf{C}^e : \mathbf{E}^e\right) \tag{11}$$

where $\psi_0^{mech} = \mathbf{E}^e : \mathbf{C}^e : \mathbf{E}^e/2$ is the elastic strain energy of current state per unit volume of the intermediate state, which is converted to a quantity based on the initial state by multiplying $J^{ch}J^{eg}$. In the above equation, $\mathbf{E}^e$ is the Green-Lagrange elastic strain tensor, defined as $\mathbf{E}^e = (\mathbf{F}^{eT}\mathbf{F}^e - \mathbf{I})/2$, $\mathbf{C}^e = h(\phi)\mathbf{C}_{MO_n}^e + (1 - h(\phi))\mathbf{C}_M^e$ is the fourth-order elasticity tensor, and the symbol ':' is the internal product between two tensor defined in Cartesian component in form of $\mathbf{E}^e : \mathbf{C}^e : \mathbf{E}^e = E_{ij}^e C_{ijkl} E_{kl}^e$.

Substituting Eqs. (10, 11) into Eq. (9), the entropy imbalance is recast as:

$$\begin{aligned} &\mathbf{P} : (\mathbf{F}^e\frac{\partial \dot{\mathbf{F}}^{cr}}{\partial t}\mathbf{F}^{ch}\mathbf{F}^{eg} + \mathbf{F}^e\mathbf{F}^{cr}\frac{\partial \dot{\mathbf{F}}^{ch}}{\partial t}\mathbf{F}^{eg} + \mathbf{F}^e\mathbf{F}^{cr}\mathbf{F}^{ch}\frac{\partial \dot{\mathbf{F}}^{eg}}{\partial t}) - \\ &(\frac{\partial \psi^{mech}}{\partial \mathbf{F}^e} : \frac{\partial \dot{\mathbf{F}}^e}{\partial t} - \mathbf{P} : \frac{\partial \dot{\mathbf{F}}^e}{\partial t}\mathbf{F}^{cr}\mathbf{F}^{ch}\mathbf{F}^{eg}) \geq 0 \end{aligned} \tag{12}$$

Using the relation involving the internal product of tensors, $\mathbf{A} : (\mathbf{BC}) = (\mathbf{AC}^T) : \mathbf{B}$, Eq. (12) can be recast as:

$$\begin{aligned} &\mathbf{P} : (\mathbf{F}^e\frac{\partial \dot{\mathbf{F}}^{cr}}{\partial t}\mathbf{F}^{ch}\mathbf{F}^{eg} + \mathbf{F}^e\mathbf{F}^{cr}\frac{\partial \dot{\mathbf{F}}^{ch}}{\partial t}\mathbf{F}^{eg} + \mathbf{F}^e\mathbf{F}^{cr}\mathbf{F}^{ch}\frac{\partial \dot{\mathbf{F}}^{eg}}{\partial t}) - \\ &(\frac{\partial \psi^{mech}}{\partial \mathbf{F}^e} - \mathbf{P}\mathbf{F}^{egT}\mathbf{F}^{chT}\mathbf{F}^{crT}) : \frac{\partial \dot{\mathbf{F}}^e}{\partial t} \geq 0 \end{aligned} \tag{13}$$

Since elastic deformation is recoverable and nondissipative, it does not induce entropy change. The elastic constitutive relation is then expressed as:

$$\mathbf{P} = \frac{\partial \psi^{mech}}{\partial \mathbf{F}^e}(\mathbf{F}^{egT}\mathbf{F}^{chT}\mathbf{F}^{crT})^{-1} = \mathbf{F}^e\frac{\partial \psi^{mech}}{\partial \mathbf{E}^e}(\mathbf{F}^{egT}\mathbf{F}^{chT}\mathbf{F}^{crT})^{-1} \tag{14}$$

According to Neto et al.[51], the first Piola-Kirchhoff stress tensor, $\mathbf{P}$, can be expressed in the form of Cauchy stress tensor, $\boldsymbol{\sigma}$, as $\boldsymbol{\sigma} = \det(\mathbf{F})^{-1}\mathbf{P}\mathbf{F}^T$, where $\det(\bullet)$ means the determinant of a matrix. Thus, Eq. (14) finally leads to:

$$\boldsymbol{\sigma} = \det(\mathbf{F})^{-1}\left(\mathbf{F}^e\frac{\partial \psi^{mech}}{\partial \mathbf{E}^e}(\mathbf{F}^{egT}\mathbf{F}^{chT}\mathbf{F}^{crT})^{-1}\right)\mathbf{F}^T \tag{15}$$

Stress dependent chemical potential

The Helmholtz free energy of the system, Ψ is an integral of the density functional, ψ, over the current configurations, Ω, which is expressed as:

$$\Psi = \int_\Omega \psi dv = \int_\Omega (\psi^{chem} + \psi^{int} + \psi^{mech})dv \tag{16}$$

where ψ is the summation of the chemical energy density, ψ^{chem}, interface energy density, ψ^{int}, and the mechanical energy density, ψ^{mech}. For the problem of inward oxide growth, we only consider the diffusion of oxygen in the oxide. Hence, the chemical energy density, ψ^{chem}, is expressed as:

$$\psi^{chem} = c_O RT\left(\ln\frac{c_O}{c_O^{ref}} - 1\right) + c_O\mu_O^0 \tag{17}$$

where c_O^{ref} is the reference concentration of oxygen dissolved interstitially in the host lattice of oxide, μ_O^0 is the standard chemical potential, and R is the ideal gas constant.

The interfacial energy density, ψ^{int}, corresponding to the energy consumed in the creation of a unit oxide-metal interface during oxidation, is expressed as:

$$\psi^{int} = \frac{\lambda}{2}|\nabla\phi|^2 + Wg(\phi) \tag{18}$$

where the first term of the right-hand side associated with the gradient of ϕ determines a diffusive interface with a finite width between metal and oxide phases and the second term is a double-well function giving an energy barrier of height W to ensure that the phases on both sides of an interface are stable. In Eq. (18), the coefficients λ and W can be related to the interfacial energy density (per unit area), s, and the interfacial thickness, δ, expressed as $\lambda = s\delta$ and $W = 18\,s/\delta$[4], respectively.

The chemical potential of a chemical component is then rationalized as the functional derivative of the total free energy to its concentration. In this work, the chemical potential of oxygen can be expressed as:

$$\mu_O = \frac{\delta \Psi}{\delta c_O} = RT\ln a_O + \mu_O^{ex} \tag{19}$$

where a_O is the activity of oxygen, which is only concentration dependent, given by:[52]

$$a_O = \exp\left(\frac{1}{RT}\left(\frac{\delta(\int_\Omega(\psi^{chem}+\psi^{int})d\omega)}{\delta c_O} - \mu_O^0\right)\right) = \frac{c_O}{c_O^{ref}} \tag{20}$$

In Eq. (19), μ_O^{ex} is the excess chemical potential that involves the contributions of mechanical energy and standard chemical potential, given by:

$$\mu_O^{ex} = \frac{\delta(\int_\Omega(\psi-\psi^{chem}-\psi^{int})d\omega)}{\delta c_O} + \mu_O^0 = \mu_O^0 + \frac{\partial\psi^{mech}}{\partial c_O} \tag{21}$$

Involving the expression of elastic strain energy density, i.e., Eq. (8), the partial derivative of ψ^{mech} with respect to c_O in Eq. (21) is expressed as:

$$\frac{\partial\psi^{mech}}{\partial c_O} = \left(\frac{\partial\psi^{mech}}{\partial\mathbf{F}^e}\frac{\partial\mathbf{F}^e}{\partial\mathbf{F}^*}\frac{\partial\mathbf{F}^*}{\partial c_O} + \frac{\partial J^*}{\partial c_O}\left(\frac{1}{2}\mathbf{E}^e:\mathbf{C}^e:\mathbf{E}^e\right)\right) \tag{22}$$

where $J^* = J^{ch}J^{eg} = \det(\mathbf{F}^*)$. In Eq. (22), the derivative of elastic strain energy density with respect to $\mathbf{F}^e$ can be expressed in the form Cauchy stress tensor, $\boldsymbol{\sigma}$, by using the relation expressed in Eq. (14), i.e.,

$$\frac{\partial\psi^{mech}}{\partial\mathbf{F}^e} = \det(\mathbf{F})\boldsymbol{\sigma}\mathbf{F}^{e-1} \tag{23}$$

The derivative of tensor, $\partial\mathbf{F}^e/\partial\mathbf{F}^*$, can be expressed in Cartesian component form as:

$$\frac{\partial\mathbf{F}^e}{\partial\mathbf{F}^*} = \left(\frac{\partial F^e_{mn}}{\partial F^*_{iJ}}\right) = \left(\frac{\partial\left(F_{mK}f^*_{Kn}\right)}{\partial F^*_{iJ}}\right) = \left(F_{mK}\frac{\partial f^*_{Kn}}{\partial F^*_{iJ}}\right) \tag{24}$$

where F^e_{mn}, $F^*_{mK(\text{or iJ})}$ and f^*_{Kn} are the components of elastic gradient tensor $\mathbf{F}^e$, inelastic gradient tensor $\mathbf{F}^*$, and its inverse $\mathbf{F}^{*-1}$, respectively. Using the relation of derivative of the inverse of a tensor[51], the Cartesian component, $\partial f^*_{Kn}/\partial F^*_{iJ}$, is expressed as:

$$\frac{\partial f^*_{Kn}}{\partial F^*_{iJ}} = -f^*_{Ki}f^*_{Jn} \tag{25}$$

Substituting Eq. (25) into Eq. (24), the derivative of tensor, $\partial\mathbf{F}^e/\partial\mathbf{F}^*$, can be rewritten as:

$$\frac{\partial\mathbf{F}^e}{\partial\mathbf{F}^*} = -\left(F_{mK}f^*_{Ki}f^*_{Jn}\right) = -\left(F^e_{mi}f^*_{Jn}\right) = -\mathbf{F}^e\mathbf{F}^{*-T} \tag{26}$$

The derivative of J^* with respect to c_O, in Eq. (22), can be expressed as:

$$\frac{\partial J^*}{\partial c_O} = \frac{\partial J^*}{\partial\mathbf{F}^*}\frac{\partial\mathbf{F}^*}{\partial c_O} \tag{27}$$

Using the relation:[51]

$$\frac{\partial J^*}{\partial\mathbf{F}^*} = J^*\mathbf{F}^{*-T} \tag{28}$$

Equation (28) is recast as:

$$\frac{\partial J^*}{\partial c_O} = J^*\mathbf{F}^{*-T}\frac{\partial\mathbf{F}^*}{\partial c_O} \tag{29}$$

Substituting Eqs. (23, 26, 29) into Eq. (22) leads to the final form of the stress-dependent chemical potential of oxygen, expressed as:

$$\mu_O = \frac{\delta\psi}{\delta c_O} = RT\ln\bar{c}_O + \mu_O^0 + \left(\psi^{mech} - \det(\mathbf{F})\boldsymbol{\sigma}\right)\mathbf{F}^{*-1}\frac{\partial\mathbf{F}^*}{\partial c_O} \tag{30}$$

It is note that the stress-dependent chemical potential involves the effects of conformational volume change and deformation energy. If the small deformation assumption is adopted, the effects of conformational volume change and deformation energy would be insignificant. Under the assumption of small deformation, Eq. (30) can be recast as:

$$\mu_O = RT\ln\bar{c}_O + \mu_O^0 - \frac{1}{c^{ref}_{MO_n}}\left(\varepsilon^{eg}_{11}\sigma_{11} + \varepsilon^{eg}_{22}\sigma_{22} + \varepsilon^{eg}_{33}\sigma_{33}\right) \tag{31}$$

Analogously, the stress-dependent of chemical potential of oxide can be expressed as:

$$\mu_{MO_n} = \frac{\delta\Psi}{\delta c_{MO_n}} = \frac{\delta\Psi}{c^{ref}_{MO_n}\delta\phi} = RT\ln a_{MO_n} + \mu^{ex}_{MO_n} \tag{32}$$

where a_{MO_n} and $\mu^{ex}_{MO_n}$ are the activity and excess chemical potential of oxide, respectively. They are derived as:

$$a_{MO_n} = \exp\left(\frac{1}{RTc^{ref}_{MO_n}}\left(W\,\partial g(\phi)/\partial\phi - \lambda\nabla^2\phi\right)\right) \tag{33}$$

and

$$\mu^{ex}_{MO_n} = \left(\psi^{mech} - \det(\mathbf{F})\boldsymbol{\sigma}\right)\mathbf{F}^{*-1}\frac{\partial\mathbf{F}^*}{c^{ref}_{MO_n}\delta\phi} \tag{34}$$

Kinetics and governing equations

Following Bazant[52] and our previous studies[7,8], the reaction rate, r, for the reaction $M + nO \rightarrow MO_n$ can be expressed as:

$$r = \frac{k^0}{a_{TS}}\left(a_R\exp\left(\frac{(1-\rho)(\mu^{ex}_R - \mu^{ex}_P)}{RT}\right) - a_P\exp\left(-\frac{\rho(\mu^{ex}_R - \mu^{ex}_P)}{RT}\right)\right) \tag{35}$$

where k_0 is the kinetics constant, ρ is the asymmetric parameter, and the subscripts 'TS', 'R' and 'P' represent the transition state, reactants and products of the reaction, respectively. The activity of transition state, a_{TS}, is set to be a constant in present work. The activity of reactants and products, a_R and a_P, are, respectively, expressed as

$$a_R = {a_O}^n = \left(\frac{c_O}{c_O^{ref}}\right)^n \tag{36}$$

$$a_P = a_{MO_n} = \exp\left(\frac{1}{RTc^{ref}_{MO_n}}\left(W\,\partial g(\phi)/\partial\phi - \lambda\nabla^2\phi\right)\right) \tag{37}$$

And the difference of excess chemical potential between reactant and products, $\mu^{ex}_R - \mu^{ex}_P$, is expressed as

$$\begin{aligned}\mu^{ex}_R - \mu^{ex}_P &= n\mu^{ex}_O - \mu^{ex}_{MO_n} = n\mu^0_O + \tau_\sigma \\ &= n\mu^0_O + n\left(\psi^{mech} - \det(\mathbf{F})\boldsymbol{\sigma}\right)\mathbf{F}^{*-1}\frac{\partial\mathbf{F}^*}{\partial c_O} - \left(\psi^{mech} - \det(\mathbf{F})\boldsymbol{\sigma}\right)\mathbf{F}^{*-1}\frac{\partial\mathbf{F}^*}{c^{ref}_{MO_n}\delta\phi}\end{aligned} \tag{38}$$

where τ_σ is the stress contribution to reaction driving force. Since the order parament is associated with concentration, defined as $\phi = c_{MO_n}/c^{ref}_{MO_n}$, the reaction rate, $r = \partial c^{ref}_{MO_n}/\partial t$, can be related to the changing rate of ϕ, i.e., $r/c^{ref}_{MO_n} = \partial\phi/\partial t$. Following our previous work[8], it leads to the following governing equation of the order parameter:

$$\frac{\partial\phi}{\partial t} = -L_\sigma\left(W\frac{\partial g(\phi)}{\partial\phi} - \lambda\nabla^2\phi\right) + L_\eta\frac{\partial h(\phi)}{\partial\phi}\left(\left(\frac{c_O}{c_O^{ref}}\right)^n\right.$$

$$\left.\exp\left(\frac{(1-\rho)(\mu^{ex}_R - \mu^{ex}_P)}{RT}\right) - \exp\left(-\frac{\rho(\mu^{ex}_R - \mu^{ex}_P)}{RT}\right)\right) \tag{39}$$

where

$$L_\sigma = \frac{k_0}{a_{TS}RT\left(c^{ref}_{MO_n}\right)^2}\exp\left(-\frac{\rho(\mu^{ex}_1 - \mu^{ex}_2)}{RT}\right) \tag{40}$$

and

$$L_\eta = \frac{k_0}{a_{\mathrm{TS}} c_{\mathrm{MO_n}}^{\mathrm{ref}}} \tag{41}$$

are the coefficients to scale the contribution of interface energy and the oxidation kinetics to phase migration, respectively.

We also give the governing equation based on the linear reaction kinetics, written as:

$$\frac{\partial \phi}{\partial t} = -L_\sigma \left(W \frac{\partial g(\phi)}{\partial \phi} - \lambda \nabla^2 \phi \right) + L_\eta^* \left(\frac{c_{\mathrm{O}}}{c_{\mathrm{O}}^{\mathrm{ref}}} \right)^n \left(\frac{n\mu_{\mathrm{O}}^0 + \tau_\sigma}{RT} \right) \tag{42}$$

where L_η^* is a kinetic constant, which is given as:

$$L_\eta^* = \frac{L_\eta RT}{\mu_{\mathrm{O}}^0} \left(\exp\left(\frac{n(1-\rho)\mu_{\mathrm{O}}^0}{RT} \right) - \exp\left(-\frac{n\rho\mu_{\mathrm{O}}^0}{RT} \right) \right) \tag{43}$$

to ensure that the reaction rate under the assumption of linear reaction kinetics is identical to that of nonlinear kinetics model (Eq. (39)), when the impact of stress ($\tau_\sigma = 0$) is ignored (note that we still consider that reaction system is highly nonequilibrium, i.e., $\mu_{\mathrm{O}}^0 \gg RT$).

The reaction-diffusion equation governing the evolution of the concentration field of oxygen is expressed as:

$$\frac{\partial c_{\mathrm{O}}}{\partial t} = \nabla \left(D \nabla c_{\mathrm{O}} - \frac{D c_{\mathrm{O}}}{RT} \nabla \left(\left(\psi^{\mathrm{mech}} - \det(\mathbf{F}) \boldsymbol{\sigma} \right) \mathbf{F}^{*-1} \frac{\partial \mathbf{F}^*}{\partial c_{\mathrm{O}}} \right) \right) - nr \tag{44}$$

where the first term on the right-hand side describes the oxygen diffusion caused by the concentration and the mechanical deformation gradients, and the second term represents the oxygen consumption (per unit time and volume) due to the reaction. D is the diffusivity coefficient, expressed as $D = p(\phi) D_{\mathrm{MO_n}} + (1 - p(\phi)) D_{\mathrm{M}}$ with $D_{\mathrm{MO_n}}$ and D_{M} being the diffusivities of oxygen atoms in the oxide and metal phases, respectively.

The stress tensor, $\boldsymbol{\sigma}$, must satisfy the equilibrium equation, expressed as:

$$\mathrm{div}(\boldsymbol{\sigma}) = 0 \tag{45}$$

where div is the divergence operator. Substituting constitutive relation Eq. (15) into Eq. (45) leads to the governing equation of deformation:

$$\mathrm{div} \left[\det(\mathbf{F})^{-1} \left(\mathbf{F}^{\mathrm{e}} \frac{\partial \psi^{\mathrm{mech}}}{\partial \mathbf{E}^{\mathrm{e}}} \left(\mathbf{F}^{\mathrm{eg}T} \mathbf{F}^{\mathrm{ch}T} \mathbf{F}^{\mathrm{cr}T} \right)^{-1} \right) \mathbf{F}^T \right] = 0 \tag{46}$$

Since the algorithm implementation methods for large inelastic deformation and mechanochemical coupling have been described by Neto et al.[51] and Loeffel et al.[39] in detail, for simplicity, the algorithm is not presented in this paper.

DATA AVAILABILITY

All data generated or analyzed during this study are included in this article (and its Supplementary Information Files).

CODE AVAILABILITY

The code that support the findings of this study are available from the corresponding author upon reasonable request.

Received: 9 January 2023; Accepted: 20 June 2023;
Published online: 05 July 2023

REFERENCES

1. Bistri, D., Afshar, A. & Leo, C. V. D. Modeling the chemo-mechanical behavior of all-solid-state batteries: a review. *Meccanica* **56**, 1523–1554 (2021).
2. Okumura, D., Kawabata, H. & Chester, S. A. A general expression for linearized properties of swollen elastomers undergoing large deformations. *J. Mech. Phys. Solids* **135**, 103805 (2020).
3. Voyiadjis, G. Z., Shojaei, A. & Li, G. A thermodynamic consistent damage and healing model for self healing materials. *Int. J. Plast.* **27**, 1025–1044 (2011).
4. Lin, C., Ruan, H. H. & Shi, S. Q. Phase field study of mechanico-electrochemical corrosion. *Electrochim. Acta* **310**, 240–255 (2019).
5. Lin, C. & Ruan, H. H. Multi-phase-field modeling of localized corrosion involving galvanic pitting and mechano-electrochemical coupling. *Corros Sci* **177**, 108900. (2020).
6. Lin, C. & Ruan, H. H. Phase-field modeling of mechano–chemical-coupled stress-corrosion cracking. *Electrochim. Acta* **395**, 139196 (2021).
7. Lin, C. & Ruan, H. H. Phase-field modeling of scale roughening induced by outward growing oxide. *Materialia* **5**, 100255 (2019).
8. Lin, C., Ruan, H. H. & Shi, S. Q. Mechano-chemical Coupling Phase Field Modeling for Inhomogeneous Oxidation of Zirconium Induced by Stress-Oxidation Interaction. *NPJ Mater. Degrad.* **4**, 22 (2020).
9. Atkinson, A. Transport processes during the growth of oxide films at elevated temperature. *Rev. Mod. Phys.* **57**, 437–470 (1985).
10. Cabrera, N. & Mott, N. F. Theory of the oxidation of metals. *Rep. Prog. Phys.* **12**, 163–184 (1948).
11. Motta, A. T., Couet, A. & Comstock, R. J. Corrosion of zirconium alloys used for nuclear fuel cladding. *Annu. Rev. Mater. Sci.* **45**, 311–343 (2015).
12. Ramsay, J. D., Evans, H. E., Child, D. J., Taylor, M. P. & Hardy, M. C. The influence of stress on the oxidation of a Ni-based superalloy. *Corros Sci.* **154**, 277–285 (2019).
13. Zhao, X. H., Feng, Y. R., Tang, S. W. & Zhang, J. X. Electrochemical corrosion behavior of 15Cr-6Ni-2Mo stainless steel with/without stress under the coexistence of CO2 and H2S. *Int. J. Electrochem. Sci.* **13**, 6296–6309 (2018).
14. Wang, X. et al. Stress-driven lithium dendrite growth mechanism and dendrite mitigation by electroplating on soft substrates. *Nat. Energy* **3**, 227–235 (2018).
15. Wellington, U. D. G. et al. Thermal barrier coatings with novel architectures for diesel engine applications. *Surf. Coat. Technol.* **396**, 125950 (2020).
16. Platt, P., Allen, V., Fenwick, M., Gass, M. & Preuss, M. Observation of the effect of surface roughness on the oxidation of Zircaloy-4. *Corros Sci.* **98**, 1–5 (2015).
17. Chen, Y. et al. A mechanistic understanding on rumpling of a NiCoCrAlY bond coat for thermal barrier coating applications. *Acta Mater.* **128**, 31–42 (2017).
18. Yu, Q. M., Zhou, H. L. & Wang, L. B. Influences of interface morphology and thermally grown oxide thickness on residual stress distribution in thermal barrier coating system. *Ceram. Int.* **42**, 8338–8350 (2016).
19. Eriksson, R. et al. TBC bond coat-top coat interface roughness: influence on fatigue life and modelling aspects. *Surf. Coat. Technol.* **236**, 230–238 (2013).
20. Dong, H., Yang, G. J., Li, C. X., Luo, X. T. & Li, C. J. Effect of TGO thickness on thermal cyclic lifetime and failure mode of plasma-sprayed TBCs. *J. Am. Ceram. Soc.* **97**, 1226–1232 (2014).
21. Lin, C. & Li, Y. M. Interface stress evolution considering the combined creep-plastic behavior in thermal barrier coatings. *Mater. Des.* **89**, 245–254 (2016).
22. Kyaw, S., Jones, A., Jepson, M. A. E., Hyde, T. & Thomson, R. C. Effects of three-dimensional coating interfaces on thermo-mechanical stresses within plasma spray thermal barrier coatings. *Mater. Des.* **125**, 189–204 (2017).
23. Lin, C., Sun, Q., Chai, Y. J., Chen, H. L. & Li, Y. M. Stress evolution in top coat of thermal barrier coatings by considering strength difference property in tension and compression. *Surf. Coat. Technol.* **329**, 86–96 (2017).
24. Busso, E. P., Evans, H. E., Qian, Z. Q. & Taylor, M. P. Effects of breakaway oxidation on local stresses in thermal barrier coatings. *Acta Mater* **58**, 1242–1251 (2010).
25. Che, C., Wu, G. Q., Qi, H. Y., Huang, Z. & Yang, X. G. Uneven growth of thermally grown oxide and stress distribution in plasma-sprayed thermal barrier coatings. *Surf. Coat. Technol.* **203**, 3088–3091 (2009).
26. Shen, Q., Yang, L., Zhou, Y. C., Wei, Y. G. & Zhu, W. Effects of growth stress in finite-deformation thermally grown oxide on failure mechanism of thermal barrier coatings. *Mech. Mater.* **114**, 228–242 (2017).
27. Li, B., Fan, X., Zhou, K. & Wang, T. J. Effect of oxide growth on the stress development in double-ceramics-layer thermal barrier coatings. *Ceram. Int.* **43**, 14763–14774 (2017).
28. Xie, F., Sun, Y. L., Li, D. J., Bai, Y. & Zhang, W. X. Modelling of catastrophic stress development due to mixed oxide growth in thermal barrier coatings. *Ceram. Int.* **45**, 11353–11361 (2019).
29. Larche, F. C. & Cahn, J. L. The effect of self-stress on diffusion in solids. *Acta Metall* **30**, 1835–1845 (1982).
30. Bucci, G., Nadimpalli, S. P. V., Sethuraman, V. A., Bower, A. F. & Guduru, P. R. Measurement and modeling of the mechanical and electrochemical response of amorphous Si thin film electrodes during cyclic lithiation. *J Mech Phys Solids* **62**, 276–294 (2014).
31. Bower, A. F., Chason, E., Guduru, P. R. & Sheldon, B. W. A continuum model of deformation, transport and irreversible changes in atomic structure in amorphous lithium–silicon electrodes. *Acta Mater.* **98**, 229–241 (2015).

32. Gao, Y. F. & Zhou, M. Coupled mechano-diffusional driving forces for fracture in electrode materials. *J. Power Sources* **230**, 176–193 (2013).
33. Haftbaradaran, H., Gao, H. & Curtin, W. A. A surface locking instability for atomic intercalation into a solid electrode. *Appl. Phys. Lett.* **96**, 091909 (2010).
34. Huang, S. & Zhu, T. Atomistic mechanisms of lithium insertion in amorphous silicon. *J. Power Sources* **196**, 3664–3668 (2011).
35. Zhou, H. G., Qu, J. & Cherkaoui, M. Stress–oxidation interaction in selective oxidation of Cr–Fe alloys. *Mech. Mater.* **42**, 63–71 (2010).
36. Wu, C. H. The role of Eshelby stress in composition-generated and stress-assisted diffusion. *J Mech Phys Solids* **49**, 1771–1794 (2001).
37. Cui, Z. W., Gao, F. & Qu, J. M. A finite deformation stress-dependent chemical potential and its applications to lithium ion batteries. *J. Mech. Phys. Solids* **60**, 1280–1295 (2012).
38. Krishnamurthy, R. & Srolovitz, D. J. Stress distributions in growing oxide films. *Acta Mater.* **51**, 2171–2190 (2003).
39. Loeffel, K. & Anand, L. A chemo-thermo-mechanically coupled theory for elastic–visco plastic deformation, diffusion, and volumetric swelling due to a chemical reaction. *Int. J. Plast.* **27**, 1409–1431 (2011).
40. Lin, C. & Li, Y. M. A coupled mechano-chemical model for reflecting the influence of stress on oxidation reactions in thermal barrier coating. *J. Appl. Phys.* **123**, 215305 (2018).
41. Zhao, Y. N., Chen, Y. F., Ai, S. G. & Fang, D. N. A diffusion, oxidation reaction and large viscoelastic deformation coupled model with applications to SiC fiber oxidation. *Int. J. Plast.* **118**, 173–189 (2019).
42. Xu, G. N., Yang, L. & Zhou, Y. C. A coupled theory for deformation and phase transformation due to CMAS infiltration and corrosion of thermal barrier coatings. *Corros Sci* **190**, 109690 (2021).
43. Zaeem, M. A. & Kadiri, H. E. An elastic phase field model for thermal oxidation of metals: application to zirconia. *Comp. Mater. Sci.* **89**, 122–129 (2014).
44. Karlsson, A. M., Levi, C. G. & Evans, A. G. A model study of displacement instabilities during cyclic oxidation. *Acta Mater* **50**, 1263–1273 (2002).
45. Steinbruck, M. & Schaffer, S. High-temperature oxidation of Zircaloy-4 in oxygen–nitrogen mixtures. *Oxid. Met.* **85**, 245–262 (2016).
46. Parry, V., Tran, M. & Wouters, Y. Detection of breakaway oxidation with acoustic emission during zirconium oxide scale growth. *Oxid. Met.* **79**, 279–288 (2013).
47. Evans, A. G., Clarke, D. R. & Levi, C. G. The influence of oxides on the performance of advanced gas turbines. *J. Eur. Ceramic Soc.* **28**, 1405–1419 (2008).
48. Xiao, B., Robertson, T., Xiao, H. & Kearsey, R. Fracture performance and crack growth prediction of SPS TBCs in isothermal experiments by crack numbering density. *Ceram. Int.* **46**, 2682–2692 (2020).
49. Tejland, P. & Hans-Olof, A. Origin and effect of lateral cracks in oxide scales formed on zirconium alloys. *J. Nucl. Mater.* **430**, 64–71 (2012).
50. Versaci R. A., Ipohorski M. *Temperature Dependence of Lattice Parameters of Zirconium* (Comision Nacional De Energia Atomica, 1991).
51. de Souza Neto E. A., Peric D., Owen D. R. J. *Computational Methods for Plasticity: Theory and Applications* (John Wiley & Sons Ltd, 2008).
52. Bazant, M. Z. Theory of chemical kinetics and charge transfer based on nonequilibrium thermodynamics. *Acc. Chem. Res.* **46**, 1144–1160 (2013).

ACKNOWLEDGEMENTS

C.L. acknowledges the support from Natural Science Foundation of Guangdong Province (2022A1515011891) and "Young Top Talents" in the Pearl River Talent Project of Guangdong Province (2021QN02L344). J.J. acknowledges the support from National Natural Science Foundation (52005523). H.R. acknowledges the financial support provided by the Hong Kong GRF (Grant No. 15213619 and 15210622) and by the industry (HKPolyU Project ID: P0039303), X.M. acknowledge the support from National Science Foundation of China (U2032143), the Guangdong Major Project of Basic and Applied Basic Research (2019B030302011).

AUTHOR CONTRIBUTIONS

C.L. was responsible for the (1) ideation (2) modeling (3) simulation implementation (4) original-writing; C.L., H.R., X.M. and J.J. were responsible for the manuscript (1) discussion (2) writing-review and (3) writing-editing.

COMPETING INTERESTS

The authors declare no competing interests.

ADDITIONAL INFORMATION

Supplementary information The online version contains supplementary material available at https://doi.org/10.1038/s41529-023-00376-z.

Correspondence and requests for materials should be addressed to Chen Lin, Haihui Ruan or Xianfeng Ma.